Exp Fluids (2015) 56:115
DOI 10.1007/s00348-015-1987-6

RESEARCH ARTICLE

Toluene-based planar laser-induced fluorescence imaging of temperature in hypersonic flows

D. Estruch-Samper[1,2] · L. Vanstone[1] · R. Hillier[1] · B. Ganapathisubramani[3]

Received: 15 December 2014 / Revised: 8 May 2015 / Accepted: 11 May 2015 / Published online: 27 May 2015
© Springer-Verlag Berlin Heidelberg 2015

Abstract Planar laser-induced fluorescence imaging is carried out in a hypersonic gun tunnel at a freestream Mach number of 8.9 and Reynolds number of $47.4 \times 10^6\ \mathrm{m}^{-1}$ (N_2 is the test gas). The fluorescence of toluene (C_7H_8) is correlated with the red shift of the emission spectra with increasing temperature. A two-colour approach is used where, following an excitation at 266 nm, emission spectra at two different bands are captured in separate runs using two different filters. Two different flow fields are investigated using this method: (i) hypersonic flow past a blunt nose, which is characterised by a bow shock with strong entropy effects, and (ii) an attached shock-wave/boundary-layer interaction induced by a flare located further downstream on the same blunt cylinder body. Measurements from as low as the freestream temperature of 68.3 K all the way up to 380 K ($T_\infty - 5.6T_\infty$) are obtained. The uncertainty at the higher temperature level is approximately ±15 %, while at the low end of the temperature, an additional ±15 % uncertainty is expected. Application of the technique is further challenged at high temperatures due to the exponentially reduced fluorescence quantum yields and the occurrence of toluene pyrolysis near the stagnation region ($T_o = 1150$ K). Overall, results are found to be within 10 % agreement with the expected distributions, thus demonstrating suitability of the technique for hypersonic flow thermometry applications in low-enthalpy facilities.

✉ D. Estruch-Samper
mpedavid@nus.edu.sg

[1] Department of Aeronautics, Imperial College London, London SW7 2AZ, UK

[2] Department of Mechanical Engineering, National University of Singapore, 117575 Singapore, Singapore

[3] Engineering and the Environment, University of Southampton, Southampton SO17 1BJ, UK

1 Introduction

Hypersonic ground testing has traditionally relied in optical methods such as schlieren imaging to visualise changes in density within the flow (Settles 2012). Optical methods offer the capabilities to perform non-intrusive measurements of the flow in regions that are difficult to access; however, the development of advanced diagnostics has proven to be particularly difficult in hypersonic facilities, where optical access is restricted and the extreme pressures and strong flow gradients, together with the inherently short test durations and fast flow speeds, pose particular challenges to such applications (Estruch-Samper et al. 2009).

Planar laser-induced fluorescence (PLIF) methods rely on probing the fluorescence of a tracer (either already present or purposely introduced in the flow) via excitation by laser light. Through calibration of the related photo-physical properties, information about the flow can be obtained. PLIF methods have particularly received attention in propulsion and combustion research for the measurement of species concentrations, which often occur naturally in combustion products, for example, hydroxyl radical (OH) and nitric oxide (NO) (Cessou et al. 2000; Rossmann et al. 2003; Sjoholm et al. 2012). Scalar properties such as density and molecular concentration can be measured through appropriate selection of a tracer/laser wavelength combination, where the laser wavelength excites a particular transition of the molecular tracer. Since fluorescence emissions generally occur in time scales within the nanosecond–microsecond range (Burton and Noyes 1968), PLIF imaging often relies in image intensifier systems, which are composed of a

photocathode, a microchannel plate and a phosphor screen in order to capture the very low light levels. This is particularly critical in high-speed flow applications where short exposures are needed to 'freeze' the flow.

A number of PLIF variances have been applied in high-speed wind tunnel testing to date including OH PLIF—used for flow visualisation in a supersonic combustion facility (Johansen et al. 2014), krypton PLIF—for scalar imaging in a supersonic underexpanded jet (Narayanaswamy et al. 2011), acetone PLIF—for measuring density distribution within a supersonic free jet (Hatanaka et al. 2012), and NO PLIF—for application in facilities where NO is naturally occurring such as in arc-heated tunnels (O'Byrne et al. 2006; Inman et al. 2011), amongst a few others. Recent research has highlighted the potential of using toluene as a PLIF tracer for flow thermography applications given its strong temperature dependence (Koban et al. 2004; Luong et al. 2006; Yoo et al. 2011; Miller et al. 2013); however, one of the main related limitations is that the photo-physics of toluene fluorescence are only documented for a very narrow range of conditions. The present study aims at investigating the applicability of the toluene PLIF technique in hypersonic experimental research, for which temperature is a driving parameter, but yet the bulk of temperature measurements to date has been restricted to the surface of the model (Anderson 2000).

2 Toluene PLIF

Toluene is an aromatic hydrocarbon and a derivative of benzene (C_6H_6) which contains the methyl group (CH_3) in the place of a hydrogen atom, hence sometimes also referred to as methylbenzene and in molecular formulation expressed as C_7H_8. Early studies on the fluorescence properties of toluene were those by Burton and Noyes (1968), where its relatively high fluorescence quantum yield (FQY) was noticed, but it was not until more recently that it saw its first applications as a PLIF tracer (Einecke et al. 2000). The majority of applications have since been in combustion research, in particular in internal combustion (IC) engine studies (Koban et al. 2005; Devillers et al. 2009; Strozzi et al. 2009). Since the absorption wavelengths of toluene are within the low UV spectrum, excitation can be achieved by means of high-power lasers such as krypton fluoride (KrF) lasers at 248 mm, quadrupled (fourth harmonic) neodymium-doped yttrium aluminium garnet (Nd:YAG) lasers at 266 nm, as well as tunable lasers. Following laser excitation, the fluorescence lifetimes of toluene are generally below about 50 ns for pure nitrogen at ambient conditions and decrease with temperature and oxygen concentration, exhibiting lifetimes shorter than 1 ns in pure air at ambient pressure and temperature (Faust et al. 2011).

An extensive characterisation of the photo-physical properties of toluene was carried out by Koban et al. (2004), who documented a consistent red shift of the emission profile with increasing temperature, and with signal intensities of three orders of magnitude lower at 900 K in comparison with those at 300 K, for both 266- and 248-nm excitation. This study thus identified the potential high temperature sensitivities of toluene PLIF, which under certain conditions were found to be even up to two orders of magnitude higher than those obtained with more commonly used PLIF variances (e.g. using acetone as a tracer). In subsequent work by Koban et al. (2005), toluene was also found to exhibit a significant decrease in emission intensity with increasing oxygen partial pressures due to the related reduction in intramolecular fluorescence lifetimes. Further studies then went on to establish oxygen concentration to be the main source of collisional quenching and determined the highest FQY conditions to occur at low temperatures and in oxygen-free environments (e.g. Luong et al. 2006; Zimmermann et al. 2006; Oehlschlaeger et al. 2007; Strozzi et al. 2009). More recently, Yoo et al. (2010) extended applicability of single-band (or single-colour) toluene PLIF to shock tube studies, which was followed by further work by Miller et al. (2013) on single- and double-band toluene PLIF temperature imaging in an expansion tube facility. The latter successful developments encouraged the present investigation.

3 Methodology

3.1 Hypersonic gun tunnel

The facility used in this study is the Imperial College gun tunnel, which was used with nitrogen as the test gas and with a contoured nozzle to produce a freestream Mach number of $M_\infty \approx 9$, with a test duration of about 25 ms and an established flow time of 6 ms (Needham et al. 1970; Mallinson et al. 2000). The facility is specifically calibrated to operate at three different pressure conditions (Table 1) that yield freestream Reynolds numbers (Re_∞) in the range of 6.5×10^6 to 47.4×10^6 m^{-1}. The high-pressure operating conditions were selected for the present application in order to ensure stronger temperature gradients and produce turbulent flows which are less prone to separate and thus

Table 1 Imperial College gun tunnel freestream flow properties for three baseline test conditions

	Low pressure	Medium pressure	High pressure
M_∞	$8.8 \pm 0.5\,\%$	$8.85 \pm 0.5\,\%$	$8.9 \pm 0.5\,\%$
$P_{0,\infty}$ (MPa)	$9.9 \pm 2\,\%$	$15.4 \pm 2\,\%$	$60.8 \pm 2\,\%$
$T_{0,\infty}$ (K)	$1040 \pm 4\,\%$	$1135 \pm 4\,\%$	$1150 \pm 4\,\%$
Re_∞ (m^{-1})	$6.5 \times 10^6 \pm 7\,\%$	$12.6 \times 10^6 \pm 7\,\%$	$47.4 \times 10^6 \pm 7\,\%$

more likely to result in simpler topologies, in comparison with flows containing large separation regions. Wall temperature was at ambient conditions $T_w = 293$ K ± 1.5 %, and the nominal isentropic freestream temperature and pressure were $T_\infty = 68.3$ K and $p_\infty = 3100$ Pa. These low values are a result of the high Mach number of the flow, and they are in much contrast to the extremely high stagnation properties ($T_{0,\infty} = 1150$ K and $p_{0,\infty} = 60.8$ MPa).

The region of core flow at $M_\infty \approx 9$ extends from the inside of the nozzle (which has an exit diameter of 350 mm) and across the test section, allowing to accommodate models of up to ~800 mm in length. The facility, which can produce run-to-run repeatability within $\pm$ 2 % variation in driver pressure (Table 1), is composed of a driver and a barrel separated by a septum chamber with two purposely designed steel diaphragms. A schematic diagram of the facility is shown in Fig. 1, where D_1 corresponds to the first diaphragm, which separates the driver from the septum, and the second diaphragm D_2 separates the septum from the barrel. A third diaphragm D_3 is located at the nozzle inlet, and near vacuum conditions ($\leq$4 mbar) are obtained in the nozzle/test section/dump tank assembly prior to the run so as to ensure sufficiently high-pressure ratios for tunnel start. During a high-pressure test, the barrel is initially filled up to a pressure of 1055 kPa, and then the driver and septum are pressurised to 46.9 MPa. The driver is then isolated and pressurised to slightly above twice this value (97.5 MPa). The tunnel is subsequently started by opening the septum isolation valve, which leads to a sudden increase in pressure followed by a rupture of the diaphragms and acceleration of the piston inside the barrel, thus compressing the test gas and leading to a rupture of the third diaphragm and to tunnel start with a freestream total pressure of $P_{0,\infty} = 60.8$ MPa. For the present study, a controlled nitrogen/toluene mixture was injected into the test gas barrel.

3.2 Two-colour PLIF thermometry

The measurements rely on the correlation between the fluorescence characteristics of toluene and the amount of oxygen and temperature of the flow under a certain range of conditions. In mixtures free of oxygen, as in this case, the photo-physical characterisation of toluene fluorescence can be simplified so that, on its own, the laser-induced fluorescence (LIF) signal S_{LIF} for a given condition can be expressed in the form:

$$S_{\mathrm{LIF}} = \frac{E}{h\nu} n_{\mathrm{tol}} \sigma(\lambda_{\mathrm{ex}}, T) \phi(\lambda, \lambda_{\mathrm{ex}}, T, P_{\mathrm{tol}}, P) \eta(\lambda) \quad (1)$$

The LIF signal therefore becomes a function of the incident number of photons $\frac{E}{h\nu}$ (where E is the fluence of the excitation laser, h is Planck's constant, and ν is the frequency of the excitation laser), the fraction of photons absorbed $n_{\mathrm{tol}}\sigma$ (which is the number density of fluorescing species, $n_{\mathrm{tol}} = P_{\mathrm{tol}}/(RT)$, times the absorption cross section, σ), the fraction of photons re-emitted as fluorescence ϕ (or FQY) and the overall efficiency of the imaging system η. While the absorption cross section is a function of excitation wavelength and temperature $\sigma(\lambda_{\mathrm{ex}}, T)$ and the efficiency of the system is a function of the fluorescence wavelength, $\eta(\lambda)$, the FQY (or ϕ) of toluene is a rather more intricate property to characterise as it is a function of the particular wavelength at which toluene fluoresces and at which it is excited, λ and λ_{ex}, as well as a function of the flow temperature and pressure, and tracer partial pressure, T, P and P_{tol}. For a given mixture, excitation wavelength and spectral filter combination, the PLIF image obtained can thus be expressed as follows, where (x,y) are the spatial locations corresponding to each pixel in the horizontal and vertical directions in the image:

$$S_{\mathrm{LIF}}(x, y, T) = E(x, y) n_{\mathrm{tol}}(x, y) \sigma(x, y) \phi(T(x, y)) \eta \quad (2)$$

By knowing E, n_{tol} and pre-documenting σ (e.g. expected to be $\sim 2 \times 10^{-19}$ cm^2 within the 300–400 K range for 266-nm excitation as per Koban et al. 2004; Cheung 2011), the region represented by each pixel in the PLIF image (x, y) can be effectively treated as an integration across each given spectral band and have its intensity correlated with temperature T. This relation permits application to constant pressure flows with homogeneous tracer distributions by means of a single-band approach, but the assumptions above do not apply to flows involving pressure changes and therefore with non-uniform tracer distributions. In such

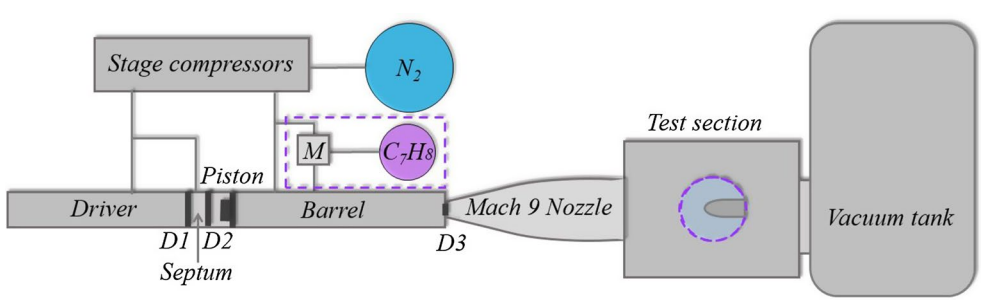

Fig. 1 Hypersonic gun tunnel schematic indicating location of the three diaphragms, $D_1 - D_3$, with additional nitrogen (N_2) and toluene (C_7H_8) mixer, M. Schematic not to scale

cases, a two-colour approach can be used, which relies in imaging the flow field using two different spectral filters, each of them imaging a different portion of the fluorescence spectrum. The filters are usually referred to as *red* and *blue* based on the part of the fluorescence spectrum they transmit, i.e. imaging of the higher wavelengths corresponds to the *red* filter and the lower wavelengths corresponds to the *blue* filter. After taking into account the efficiency of the filters for a particular imaging system, which is also a function of wavelength $\eta(\lambda)$ (including camera quantum efficiency, overall transmission of the optics, etc.), the ratio of the two corresponding signal intensities, S_{red} and S_{blue}, can be expressed as follows:

$$\frac{S_{red}}{S_{blue}} = \frac{E(x,y)n_{\mathrm{tol}}(x,y)\sigma(T(x,y))\phi(T(x,y))_{red}}{E(x,y)n_{\mathrm{tol}}(x,y)\sigma(T(x,y))\phi(T(x,y))_{blue}} \tag{3}$$

Therefore, by calculating the ratio between the two images, most of the variables cancel each other and the LIF signal at a given pixel in the image becomes a function of the ratio of FQY captured by each filter. This ratio together with an appropriate calibration leads to:

$$\frac{S_{red}(x,y,T)}{S_{blue}(x,y,T)} = cnt\frac{\phi(T(x,y))_{red}}{\phi(T(x,y))_{blue}} \tag{4}$$

The combination of two suitable filters determines the sensitivity of the relation between the PLIF signal ratio and temperature. In this study, due to limited infrastructure, a one-camera set-up was used and the *red* and *blue* images were taken in two separate runs. This implies that factors such as the flow conditions, toluene mixing, laser intensity and sheet spatial uniformity had to be repeatable from run to run. Therefore, two test cases were selected for which the flow was fully steady and highly repeatable between runs, which had been extensively investigated from a numerical and experimental approach using thin-film heat transfer sensors, fast-response pressure transducers and high-speed schlieren imaging (e.g. see Fiala et al. 2006; Estruch-Samper et al. 2012). Given the short test durations (6 ms established flow) and the low laser frequency (15 Hz), a single image per tunnel firing was obtained and three repeat runs were performed per filter and per case.

3.3 Experimental rig

The test model consisted of a blunt cylinder with a spherical nose of radius 25 mm (Fig. 2a). Test case 1 used the blunt nose section (total length of 101 mm) attached to a 66-mm-long cylinder with a diameter of 75 mm. For test case 2, the blunt nose was attached onto a 279-mm-long cylindrical section and an 8° flare model was positioned with its leading edge at $x = 212$ mm. The low flare angle was designed to result in an attached shock-wave/boundary-layer interaction (SWBLI) under turbulent flow conditions, which were produced by a uniform roughness strip of 120 μm height and located at $x = 38$ mm along the circumferential direction on the nose.

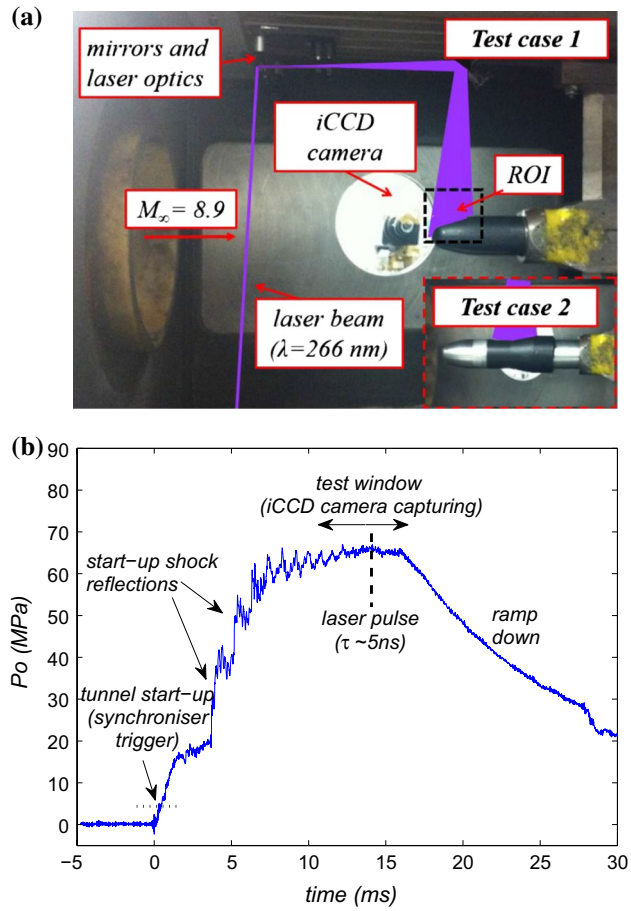

Fig. 2 Photograph of experimental rig including schematic (**a**) and gun tunnel total pressure trace indicating different stages of a high-pressure run as per present tests (**b**)

Due to limitations in optical access, the laser-sheet forming optics had to be placed inside the test section, although outside the hypersonic jet. Optics included a biconvex lens (25.4 mm diameter and 550 mm focal length) and a round cylindrical plano-concave lens (15 mm diameter, 25 mm focal length) as well as a set of round mirrors to adjust the laser path from its entry point through a small window at the bottom of the test section. All the optics were made of fused silica and had a special coating to enhance transmission within the range 248–355 nm. An intensified CCD camera (Princeton Instruments, 512 × 512 pixels, Gen II with P43 phosphor plate) was externally triggered and gated for the duration of the established flow run, with no hardware binning; a UV camera lens kit (Nikon, UV-105 mm) was used to image a field of view of 77.95 mm × 77.95 mm with a resolution of 3.271 px/mm. An Nd:YAG laser with

266-nm excitation was selected given that this wavelength has been reported to result in fluorescence signals of over an order of magnitude higher than with 248-nm excitation. The collimated laser plane at the location of the model was 60 mm wide and 1 mm thick, with a laser fluence <100mJ/cm^2, thus falling within the linear regime as per the calibrations by Yoo et al. (2010), in which a 5 % deviation in the fluorescence response was noted at about 150 mJ/cm^2. The laser was triggered using the start of the run as a reference and timed to excite the flow at the middle of the established flow window (i.e. 13 ms from trigger) following the ramp-up to steady test conditions and prior to the subsequent ramp-down (Fig. 2b). In order to obtain constant excitation energy levels, the laser was kept warm by running it externally at 15 Hz until immediately before the run, by which point the shutter was reset to wait for the tunnel start-up trigger. In addition to the anti-reflective tape on the model (Shurtape high-performance black masking tape), a very efficient means to minimise reflections with the present cylindrical configuration was to offset the laser plane 1 mm behind the centreline of the model, resulting in related errors of ~4 % in the freestream and ~1 % downstream of the bow shock.

A toluene seeding system made use of a Bronkhorst controlled evaporation mixing (CEM) unit with Coriolis flow meter. This system allowed injecting a controlled mixture of nitrogen and toluene into the tunnel barrel through accurate control of the nitrogen and toluene mass flow rates into the mixing chamber. Spectrophotometric-grade toluene with high purity was used (Sigma-Aldrich), and the mixture was set with a molar mass concentration of 1.0 % of toluene in nitrogen, corresponding to a toluene partial pressure of 4 mbar, which proved to yield sufficiently high signal intensities within the temperature range of interest and is well below the saturation pressure of toluene (~50 mbar at ambient temperature). Although toluene poses reduced risk in comparison with other PLIF tracers such as acetone, the amount used was limited in part to help minimise long-term exposure levels and given the requirement for enhanced ventilation in the facility for higher tracer concentrations.

The present PLIF results are also compared with heat transfer measurements on test case 2 (SWBLI). For such measurements, temperature gauges were designed in house to fit the cylindrical body and the flare which allowed capturing both the upstream and downstream regions of the interaction ($x = 183$ mm to $x = 244$ mm). The output of the gauges was amplified and low-pass-filtered at 50 kHz before being digitised by a 16-bit analogue-to-digital converter at a sample rate of 100 kHz for each channel. Heat transfer was calculated using the theory of Schultz and Jones (1973), resulting in a measurement error of heat transfer of ±10 % (including a ±5 % uncertainty in the substrate thermal properties, a ±1 % uncertainty related to the thin-film thermo-resistive properties, and a ±4 % regarding calibration of the gauges, signal conditioning and spatial resolution). High-speed schlieren visualisations were also obtained with a Photron Fastcam SA1.1 high-speed camera at a frame rate of 100,000 fps and using a Z-type schlieren optical arrangement.

4 PLIF signal calibration

Given the difficulties in calibrating in-situ due to the large size of the nozzle/test section/dump tank assembly ($V \approx 20\,\mathrm{m}^3$) and the limitations to use relatively small amounts of toluene within the facility, the calibration exercise was carried out in a static cell ($V \approx 0.02\,\mathrm{m}^3$) in which the nitrogen/toluene mixture was injected by means of the same system used in the main tests (Sect. 3.3). In this case, an intensified CCD (iCCD) spectrometer was used (Princeton Instruments iCCD, 600 line mm^{-1} grating) to obtain spectral measurements within the 265–322-nm range and with a resolution of 0.2 nm (with effectively two-point hardware binning). The selection of this spectral range was determined in earlier investigations using a coarser resolution and wider spectral range. The dependence of the LIF signal on pressure was initially assessed by monitoring the change in the spectral profile as pressure was decreased from just above atmospheric conditions to near vacuum pressures. The corresponding trends are shown in Fig. 3a, where the fluorescence signal appears in the range 266–322 nm and appears to decrease from about 560 mbar to the lowest pressure conditions (down to 13 mbar in this calibration run).

The trend exhibits two peaks at 277 and 282 nm, as well as the 266-nm peak which corresponds to the excitation wavelength. In Fig. 3b, the same data is presented in non-dimensional form with respect to the intensity at 282 nm for each case (corresponding to the maxima in the spectra). For the present calibrations at room temperature, the same profile is maintained across the spectral range, suggesting that vibrational relaxation and collisional quenching of toluene by molecular nitrogen remain negligible; the only exception to this is found near the excitation wavelength (266 nm), where the peak is found to increase in intensity and broaden across the spectral range as pressure is decreased. This tendency seems to be correlated with the overall signal quenching effect with decreasing pressure and is mostly noticeable at pressures below ~500 mbar (Fig. 3a).

The dependence on temperature was subsequently investigated by heating up the mixture and the insulated test cell to 380 K. In Fig. 4, this increase in temperature is shown to result in a red shift of the fluorescence spectral profile of approximately 2–3 nm with respect to the FQY at ambient

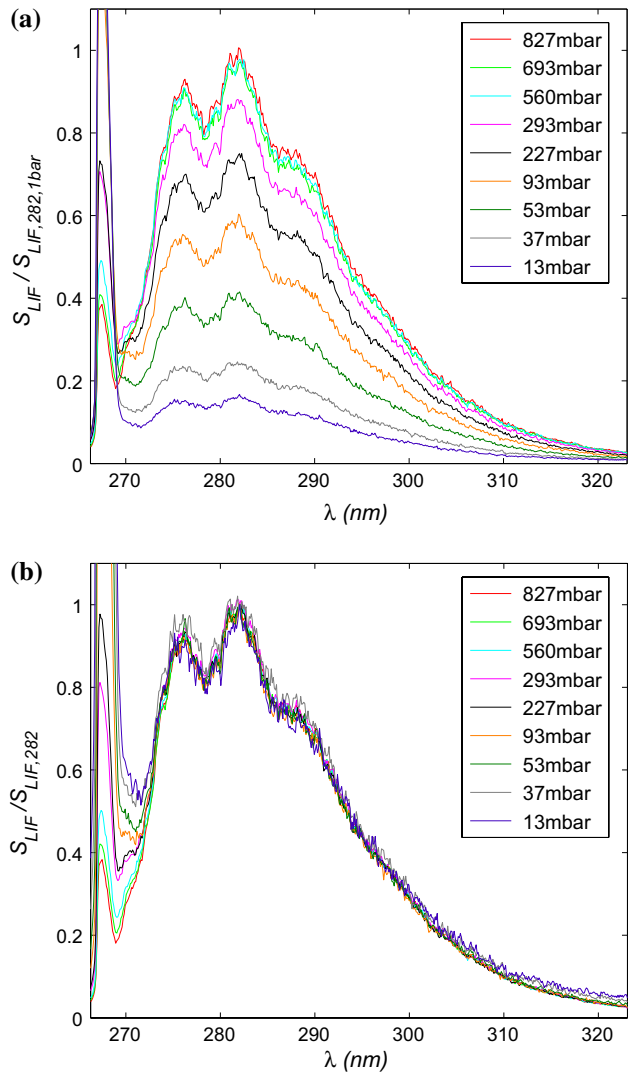

Fig. 3 LIF signal spectra for different pressures (13–827 mbar) and normalised by intensity at 282 nm for 1 bar conditions (**a**), and corresponding trend with respect to the LIF intensity at 282 nm for each individual case (**b**)

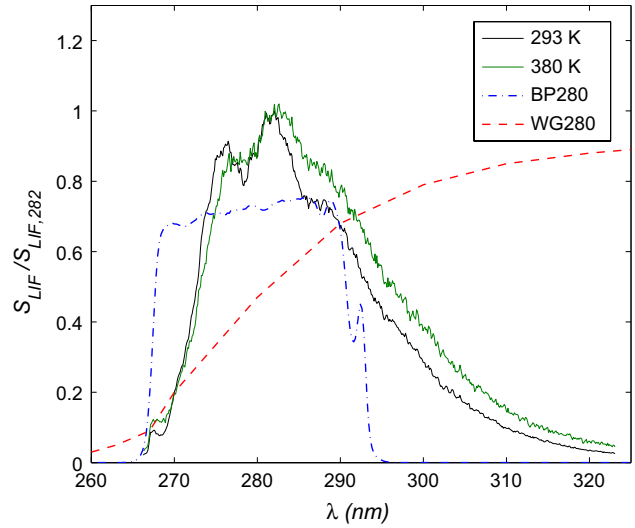

Fig. 4 Toluene fluorescence spectra at atmospheric conditions, $T = 293$ K, and at a temperature of 380 K with corresponding shift in the spectral profile, with respect to 282 nm, and indicating manufacturer-provided filter curves

conditions ($T_{amb} = 293\,K \pm 1.5$), with the shift being more noticeable towards the upper half of the profile >282 nm) and the lower side being less sensitive to temperature. A band-pass filter of the type BP280 (Semrock FF01-280/20-25), centred at 280 nm with a nominal band pass of 280 ± 10 nm, was used to image the left side of the profile (*blue* filter), and a long-pass filter (Schott N-WG280) with cut-off at about 280 nm, but with a more gradual rising edge, was used to capture the right side of the profile (*red* filter). The nominal transmission curves for each filter (Fig. 4) show that the *blue* filter has a sharper profile with about a 3-nm rising edge and 5-nm falling edge, with a transmission of around 70 %; on the other hand, the *red* filter is expected to reach a higher transmission of up to 90 %, but its nominal rising edge spans over the present spectral profile with minor transmission starting just above 266 nm.

For a more accurate calibration of this filter pair, the signal captured through each of them was measured at ambient temperature and for a range of sub-atmospheric pressures (Fig. 5). Measurements confirmed that the *blue* filter profile is not far from what would be expected based on the nominal profile, with about 10 % higher transmissivity than expected; on the other hand, the *red* filter profile reveals unexpectedly a very sharp rising edge at around 275–277 nm. It may be speculated that the difference between the nominal and the measured filter trends may be due to a conservative measure of the nominal profiles; however, given the narrow ranges of toluene fluorescence, such effects are likely to induce a significant error in calibrations based on nominal profiles. It is also noticed that the *blue* filter cuts off efficiently the laser wavelength at 267 nm and the *red* filter at 275 nm. However, as a peak near the excitation wavelength becomes more prominent and broadens across the spectral range at the lowest pressures, the resulting fluorescence intensity cannot be fully blocked by the *blue* filter. For example, at 290 and 160 mbar (Fig. 5b, c), its influence is relatively low, but at the lowest pressures (20 mbar), it accounts for about 10 % of the total signal. Similar measurements at higher temperatures (380 K) suggest that this effect still persists. While bearing in mind the current limitations in characterising toluene fluorescence at extremely low pressures, it may be speculated that the increase in signal intensity at near-excitation wavelengths may be related to an increase in toluene droplet size as pressure is reduced (i.e. higher intensity of light is scattered

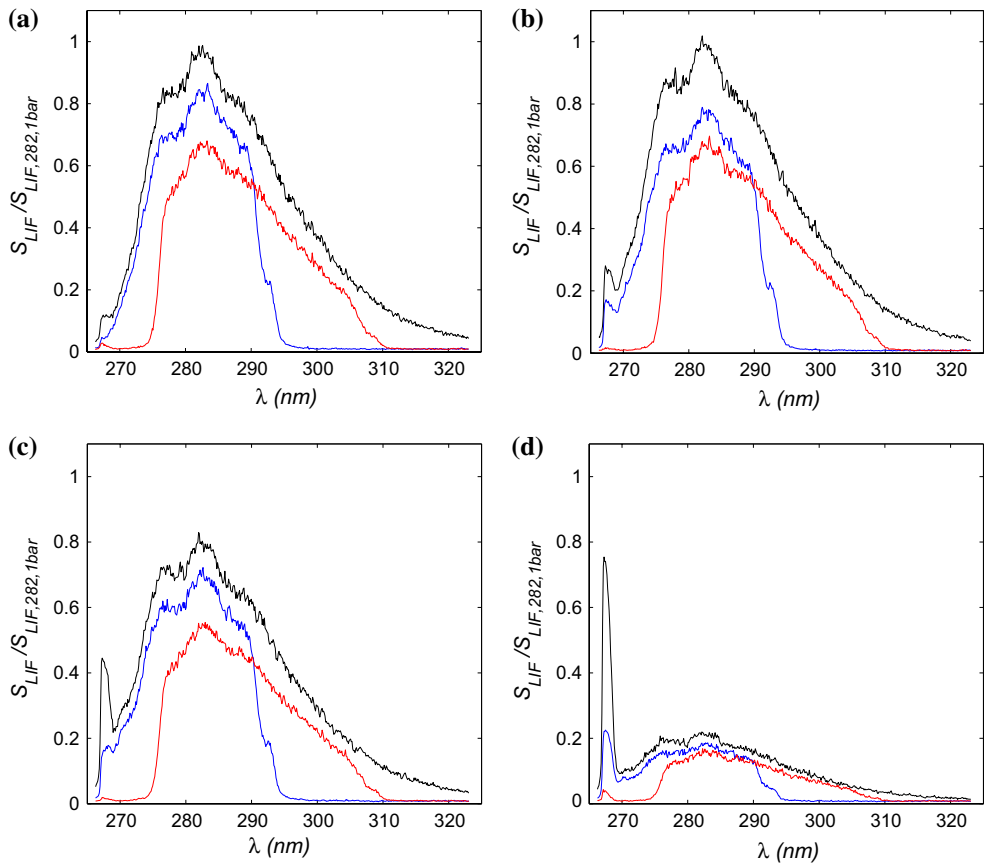

Fig. 5 Toluene fluorescence spectra comparing total fluorescence signal and that captured with the *blue* and *red* filters. Data presented for the following pressure conditions: 1000 mbar (**a**), 290 mbar (**b**), 160 mbar (**c**) and 20 mbar (**d**)

by larger toluene droplets); however, the nature of this effect cannot be fully ascertained due to the complexity of the matter and current limitations. In practice, the *blue* signal is found to be artificially higher; for the present mixture and with reference to atmospheric conditions $S_{\mathrm{LIF,atm}}$, it increases exponentially in intensity with decreasing pressure from below about 500 mbar as shown in Fig. 6, with the percentage of LIF signal intensity increase here found as $\Delta S_{\mathrm{LIF}} \approx S_{\mathrm{LIF,atm}}(1.28p^{-0.04} - 1) \times 100$ (%), with pressure expressed in mbar.

It is noted that the highest related errors are below 12 % and are only found at the low end of the pressure range, which would correspond to the freestream conditions in most applications and can therefore be easily predicted; farther downstream, the increase in pressure across a shock would also result in lower related errors. A possible solution would require designing a custom optical filter to cut off wavelengths just below 269 nm in order to ensure that there is enough spectral range for the *blue* filter to still be efficient.

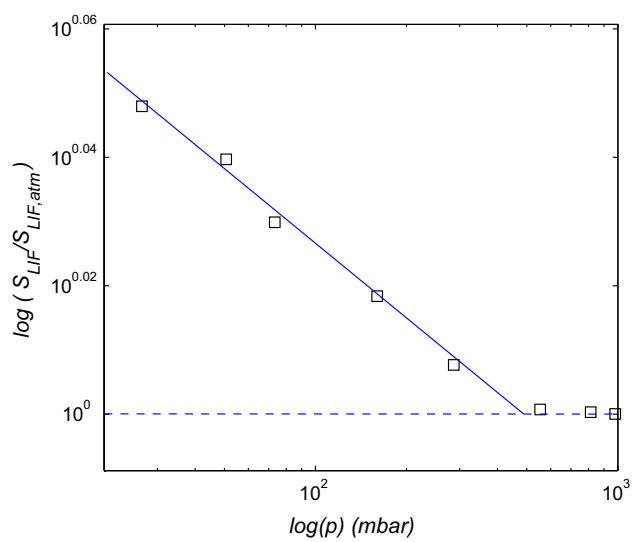

Fig. 6 LIF signal related to peak near excitation normalised by corresponding signal at atmospheric conditions and as a function of pressure. For present mixture

One of the difficulties in the present study relied on obtaining high-accuracy and sharp filters within the range of toluene fluorescence, together with the unknowns that come with nominal filter specifications before being actually calibrated. The selected filter (BP280) was chosen as the most suitable option; the same filter has also been used in the majority of past studies discussed in the literature. Another alternative in this respect could also be to excite the flow at lower wavelength, although this would come at the cost of significantly lower FQY and poor signal-to-noise ratios (SNR), thus likely leading to significantly higher errors.

The temperature calibrations for the present filter combination found that within the 293–380 K range, an 8 % increase in intensity was obtained with the *red* filter (S_{red}) while the total intensity revealed about a 3 % decrease in the *blue* filter signal (S_{blue}), i.e. with an overall increase in S_{red}/S_{blue} ratio of 11 % within the 87 K temperature increase. Further comparison with earlier studies using 266-nm excitation is shown in Fig. 7, where the practically linear relation between temperature and PLIF ratio up to approximately 500 K can be observed for a number of filter combinations (e.g. Koban et al. 2004; Miller et al. 2013). For example, in the latter study by Miller et al. (2013), the WG305 filter was chosen due to its wider spectral range (i.e. higher imaged intensity) and significant temperature sensitivity in combination with a BP280 filter. The selection of the WG280 filter for the present study was based on the need for a broader spectral range so as to obtain higher signal intensities and SNR ratios, at the cost of a small decrease in temperature sensitivity in comparison with the earlier combination.

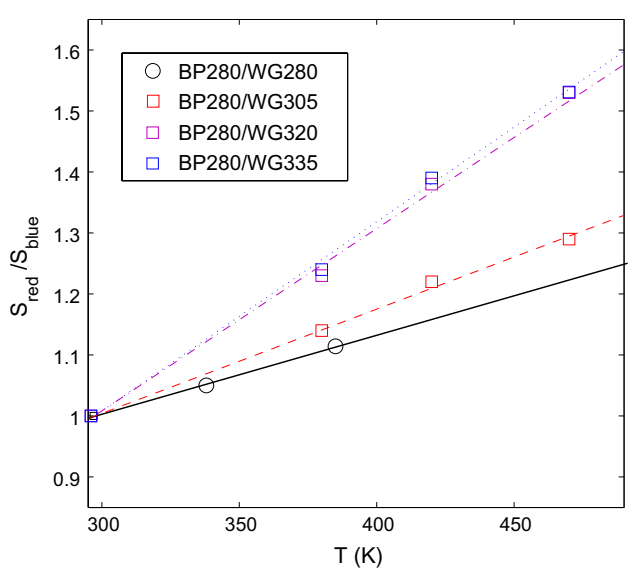

Fig. 7 LIF signal ratio S_{red}/S_{blue} as a function of temperature for present calibrations (BP280/WG280) and comparing to BP280/WG305, BP280/WG320 and BP280/WG335 from Koban et al. (2004)

Due to the lack of documentation on toluene fluorescence photo-physics, little is known on its properties at sub-atmospheric temperatures and calibration at such low temperatures (down to 68.3 K) was not deemed possible. Given the demonstrated high linearity of the PLIF signal for temperatures up to 500 K, we assume that the same linear trend could be maintained for temperatures in the bottom half of the range. In this manner, following calibration of the system efficiency response, correction for background and dark noise signal based on pretest image subtraction and application of a spatial filter (4 × 4 binning) with the purpose of effectively doubling the SNR (Yoo et al. 2010), the images were eventually overlapped and correlated with temperature using a MATLAB routine based on the procedures described in Sect. 3. Further assessment of the related experimental errors and uncertainties is discussed in the following section along with the results.

5 Hypersonic toluene PLIF results

Raw PLIF data on the blunt nose case (test case 1) are presented in Fig. 8a, b, which correspond to the *blue* and *red* images, respectively. In both images, the location of the bow shock ahead of the nose can be clearly seen, with significantly higher contrast across the shock in the *red* image. Note that the intensity of the *red* image in Fig. 8b has been increased to approximately match the intensity downstream for better clarity. In both cases, the higher density and temperature downstream of the shock wave result in an increase in intensity through it, partly due to higher toluene density.

Following post-processing of the image pair, the distribution of temperature around the blunt nose is obtained as presented in Fig. 9a. The locations of the camera field of view (FOV) and the laser sheet are indicated in Fig. 9b. It must be noted that results at the two edges of the laser sheet are discarded, so that the effective width of the FOV becomes $w_{\mathrm{las,eff}} = 42$ mm. Within this effective region, the related uncertainty is about ±2 %.

Extensive attempts were made to capture the flow at the nose, and it was concluded that measurements could not be obtained further upstream of the selected region ($x < 15$ mm, white-line shaded area in Fig. 9a), partly as a result of the high temperatures in the stagnation region ($T_o = 1150$ K) exceeding the pyrolysis temperature of toluene from about 900 K (D'Alessio et al. 2002) and also due to the relatively low signal intensities at high temperatures. Previous studies on this configuration established that the flow passing through the stagnation region remains mostly contained within the boundary layer (Fiala et al. 2006), and

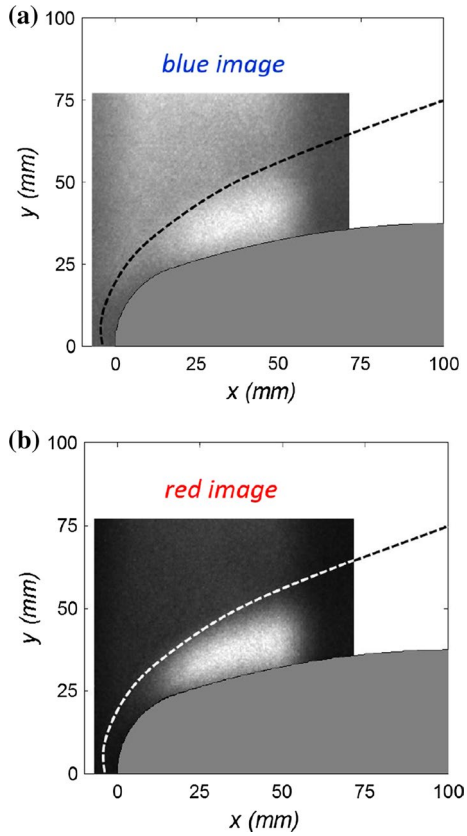

Fig. 8 Raw PLIF images on test case 1 (hypersonic blunt nose): *blue* image (**a**) and *red* image (**b**). Relative intensity of *red* image increased ×3 times for presentation purposes

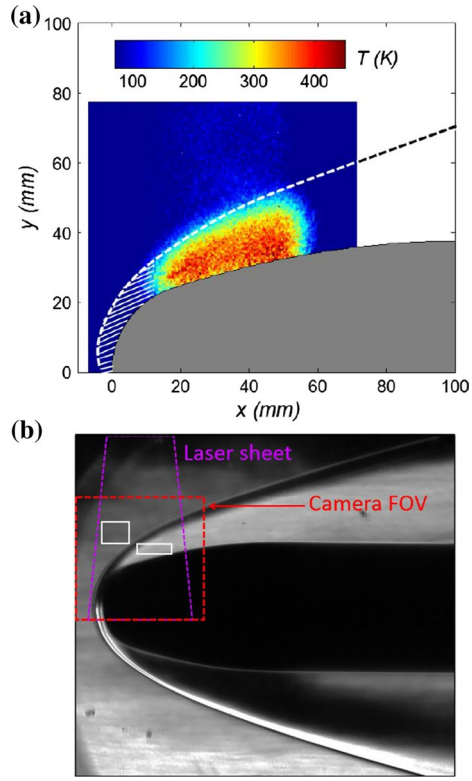

Fig. 9 Toluene PLIF results on test case 1 (**a**) and corresponding schlieren visualisation indicating location of laser sheet, camera field of view (FOV), and regions 1 ahead of shock and 2 downstream of it, shown as white squares (**b**)

as such, toluene having gone past the potentially pyrolysing temperatures at stagnation remains very close to the wall (boundary layer thickness δ is only 0.4 mm at $x = 38$ mm). Therefore, the likely formation of soot particles and carbonaceous structures at stagnation (D'Alessio et al. 2002) does not affect the results.

Downstream of stagnation, the bow shock in the PLIF image is well captured, where regions ahead of and behind it can be clearly identified. Temperature profiles within the entropy layer display an increase of 15 % over the wall temperature at a location of approximately 7 mm from the surface. This is followed by a gradual decrease in temperature at distances further away from the wall and up to the location of the shock wave, upstream of which freestream temperature conditions are reached (Fig. 10).

PLIF results on the flare-induced SWBLI (test case 2) are presented in Fig. 11a along with the corresponding schlieren visualisation in Fig. 11b. The temperature in the region ahead of the interaction is found to be ~275 K, and it increases to about 355 K downstream of the shock; the prediction of the shock-wave location is further corroborated

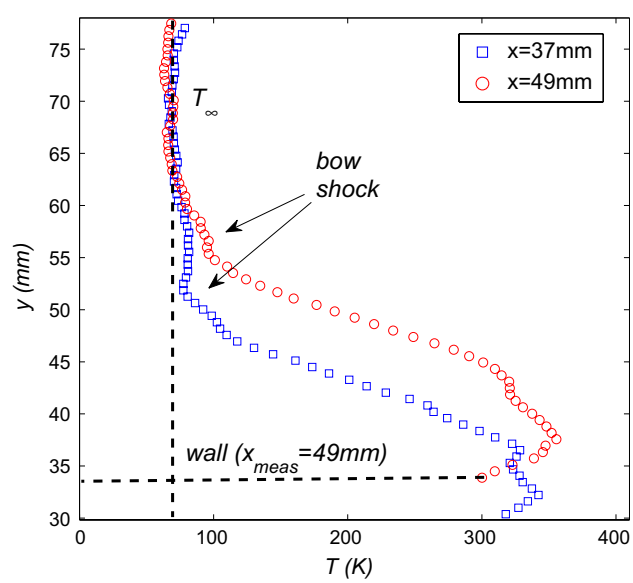

Fig. 10 PLIF temperature profile along the entropy layer at measurement locations $x = 37$ and 49 mm (with 4-by-4 px averaging)

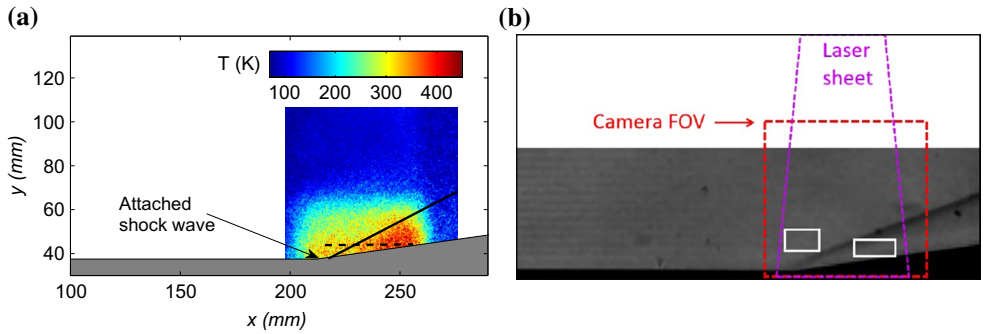

Fig. 11 Toluene PLIF results on test case 2, flare-induced interaction (**a**) and corresponding schlieren visualisation indicating laser sheet, camera field of view (FOV) and regions 3 ahead of shock and 4 downstream of it, shown as white squares (**b**)

by the schlieren image, where the shock is shown to be at an angle of 21° with respect to the freestream. As expected, temperatures close to the freestream value are also obtained at about 35 mm from the wall, that is, downstream of the upper part of the nose bow shock where flow temperature across the shock has increased minimally. It must also be noted that the interaction is submerged within the entropy layer and that the low temperatures far from the wall lies outside this layer.

Further analysis on the SWBLI case is presented in Fig. 12a where the temperature across the shock is compared to numerical predictions. For comparison with surface heat transfer measurements, a location parallel to the wall ahead of the flare is selected ($y = 45$ mm). The predicted temperature increase along this line results in an increase of 45 K (from 280 to 325 K), which takes place over a length of 4 mm. The corresponding thin-film heat transfer measurements along the wall are presented in Fig. 12b, together with the numerical predictions for temperature and heat transfer. Comparison of the PLIF temperature measurements with thin-film heat transfer measurements shows that both the temperature and heat transfer exhibit an increase along the interaction, which takes place along an axial distance of about 4 mm, i.e. with a gradient of ~11.25 K/mm and ~1.5 (W/cm^2)/mm, respectively. This relatively gradual increase, in contrast to the more immediate increase expected for canonical two-dimensional SWBLIs, is in great part due to the strong entropy layer effects, as also shown in the CFD.

Regions upstream and downstream of the shock for the two test cases were selected for further analysis. A listing of the regions can be found in Table 2, and these regions are also shown in the schlieren images (Figs. 10b, 12b) as white squares. These regions were selected to assess the quality of temperature measurements across the shock along regions with near-uniform temperature distribution. The increase in signal across the shock for the four selected regions and for the different repeated runs for each case is presented in Fig. 13a. Here, S_a and S_b are the signal intensities ahead of and behind the shock, respectively. Repeatability in terms of ratios across the shocks

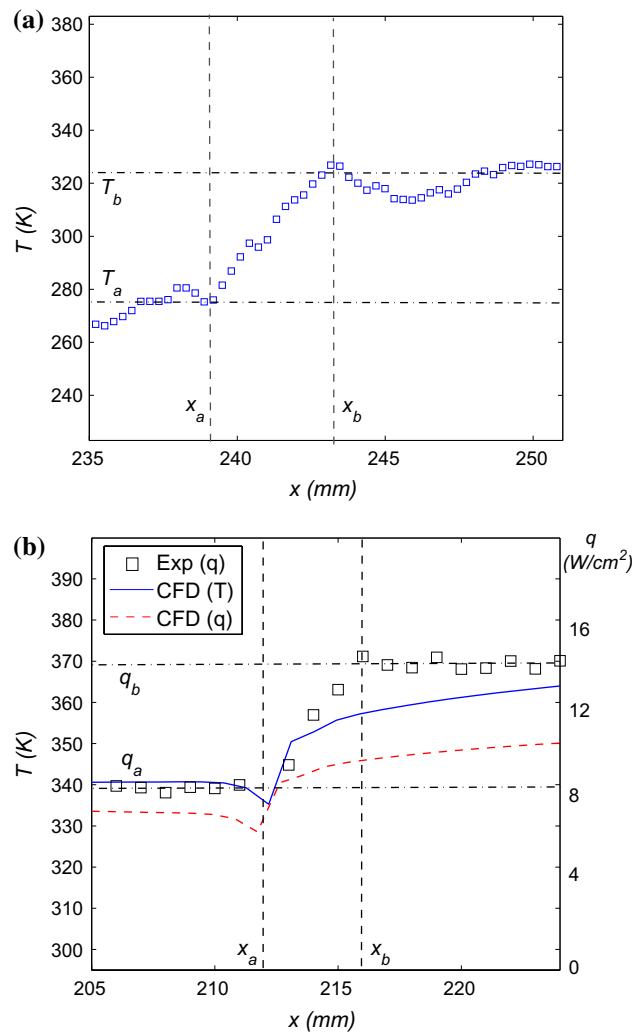

Fig. 12 PLIF temperature profile in flow near to surface ($y = 45$ mm) along SWBLI (**a**) together with surface heat transfer measurements, and numerical predictions of temperature and heat transfer (**b**). Subscripts b and a indicate conditions and reference locations *behind* and *ahead* of shock

is found to be within ±1 %. In terms of overall intensity, a higher uncertainty (5 %) related to variation in the laser excitation energy is found, mainly due to the variation in

Table 2 Properties at the four selected regions

Region	Location	$\sigma_{S_{\mathrm{LIF}}}/(S_{red}/S_{blue})$	T (K)	$S_{\mathrm{LIF}}/S_{\mathrm{LIF,atm}}$	T_{corr} (K)
1	Upstream of nose bow shock	0.095 ± 0.005	41.4 ± 40 %	11.6 %	68.3 ± 2 %
2	Downstream of nose bow shock	0.055 ± 0.005	317.5 ± 25 %	2.6 %	325.7 ± 15 %
3	Upstream of flare SWBLI	0.095 ± 0.005	249.1 ± 25 %	9.9 %	277.1 ± 15 %
4	Downstream of flare SWBLI	0.070 ± 0.005	345.0 ± 25 %	7.4 %	354.0 ± 15 %

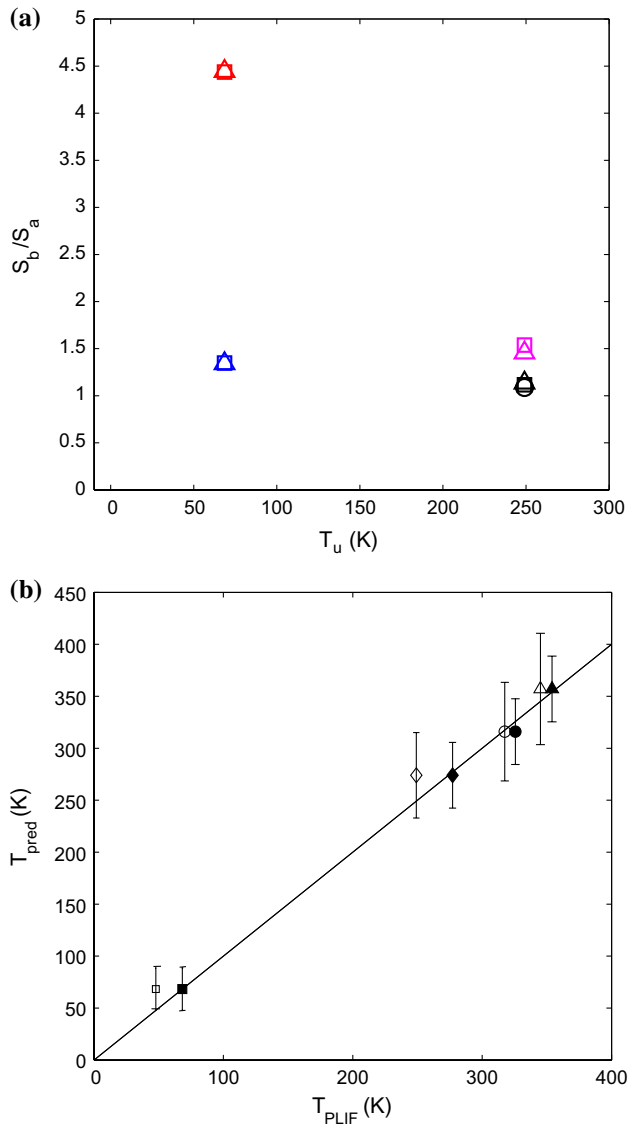

Fig. 13 LIF signal ratios across shock (S_b/S_a) for regions 1–4 where subscripts **b** and **a** indicate conditions *behind* and *ahead* of shock, respectively, for different runs and colour code: blue (*blue* filter case 1), *red* (*red* filter case 1), *black* (*blue* filter case 2), *magenta* (red filter case 2) with different symbols per run (*a*). Second image shows comparison of predicted temperatures T_{pred} and corresponding PLIF measurements T_{PLIF} with symbols indicating: *squares* (region 1), *circles* (region 2), *diamonds* (region 3) and *triangles* (region 4), *empty symbols* indicate direct T values and *solid symbols* include near-excitation scattering correction *(b)*

tunnel start-up (which is triggered by the rupture of two diaphragms and varies depending on the material and corresponding machining), thus resulting in different laser warm-up times. The lower sensitivity to temperature of the *blue* filter is also reflected in Fig. 13a; therefore, for both cases, the increase in LIF signal is larger with the *red* filter.

The temperature measurements in both regions yield values of 41 K upstream of the shock wave (region 1) and 318 K downstream of it (region 2). The freestream pressure is analytically calculated from isentropic relations, and it is found to be 31 mbar, which is the lowest pressure within the flow; the pressure in the region of interest downstream of the shock is significantly higher ($\sim$ 250 mbar based on the numerical simulations) so that the increased scattering effects near the excitation wavelength are expected to be relatively low (11.6 and 2.6 % of the total intensity of the image in these two regions). Accordingly, the corrected temperature measurements (T_{corr}) are 68.3 K (nominal value) and 325.7 K.

Across the SWBLI, the measured temperatures are 249 K (region 3) and 345 K (region 4). The predicted pressures in this case are of 45 mbar upstream and 80 mbar downstream of the shock so that the error due to increased FQY near excitation is expected to account for 9.9 and 7.4 % of the *blue* signal. The corrected temperature values (T_{corr}) are therefore 277 and 354 K. Taking into account the different uncertainties that have been mentioned, the total measurement error at near ambient conditions is found to be about 15 %, including a 2 % error related to laser profile, 5 % due to uncertainty in excitation energy and an 8 % error related to calibration of the signal ratio for the filter pair (the latter including spectrometer, iCCD imaging and temperature measurement uncertainties). This error may increase by around 10 % due to higher signal intensity near the excitation wavelengths at the lowest pressures, i.e. a total of 25 %. The highest error is expected at the lowest temperature (in the freestream) given the assumption of linearity; in this case, an additional 15 % error is accounted for. Therefore, the total error of 30 % is expected; however, this can be easily corrected based on nominal freestream values.

Comparison of the overall results for T and T_{corr} at the four locations with the expected analytical and numerical predictions in Fig. 13b shows that agreement lies within

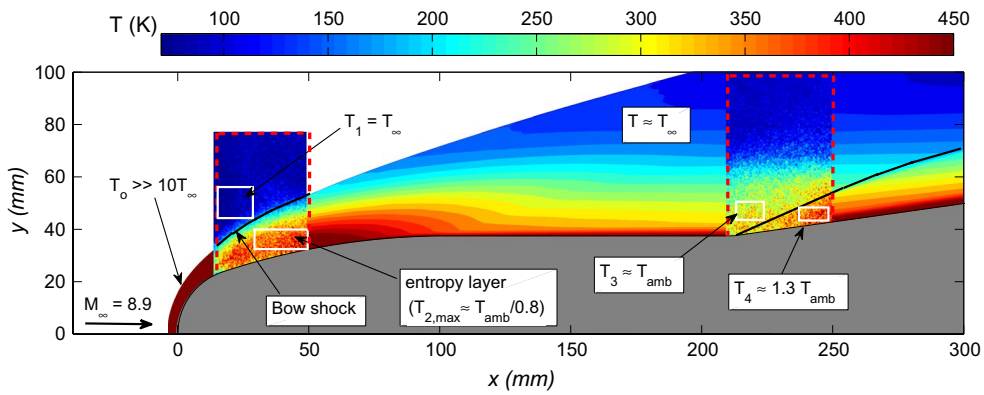

Fig. 14 Summary of present toluene PLIF application on a blunt hypersonic body with a flare indicating the main regions investigated and qualitatively compared to CFD

10 % for all cases, namely: region 1 (upstream of nose bow shock), region 2 (downstream of nose bock shock), region 3 (upstream of flare SWBLI) and region 4 (downstream of flare SWBLI). Results suggest that the assumption of linearity for sub-atmospheric temperatures is reasonable yet subject to increased errors, with freestream temperature being subject to the highest relative error, in great part due to its extremely low value. The linearity of the trend is thus likely to deviate at temperatures below 180 K, by which point toluene is expected to desublimate, thus slightly changing its FQY characteristics.

A summary of the main findings is presented in Fig. 14, where the results for the two cases are shown together with the numerical temperature contours for the whole blunt cylinder/flare body. Qualitative comparison shows that the method predicts accurately the location of shock waves and the temperature of the flow field in intricate regions such as in the strong entropy layer downstream of the bow shock (test case 1) and in the flare-induced SWBLI farther downstream (test case 2). With the appropriate modifications to optical access in the facility, larger regions could be imaged and results over larger regions could potentially be obtained. In the same way, near-wall measurements could also be performed as long as the stagnation temperature remains below 900 K.

6 Conclusions

The applicability of the toluene PLIF technique for imaging of temperature in low-enthalpy hypersonic facilities has been assessed. A one-camera system was used with the *red* and *blue* spectral filters in two successive runs, providing one image per run. The ratio of the resulting images was then correlated with temperature as in a two-colour approach. The main appeal of using toluene as a tracer is its strong temperature dependence and high FQY, which makes it particularly suitable for thermometry applications in oxygen-free environments. The 266-nm excitation provides relatively high FQY, but the proximity of this wavelength to the toluene emission spectra results in artificially increased PLIF signal which is challenging to avoid within the *red*-to-*blue* filter combination; this effect is of the order of 10 % at the lowest pressure conditions and can be taken into account with appropriate corrections. High temperatures occurring in stagnation regions in high Mach number flows are outside the range of the technique due to toluene pyrolysis effects and reduced FQYs; however, larger amounts of toluene could yield measurements in regions with temperatures as high as 900 K.

The total measurement error of the technique was found to be 15 %, with an additional 15 % at the lowest temperatures due to the assumption of linearity at the bottom of the range and due to the significantly lower absolute values. With further characterisation of toluene photo-physics and refinement of the technique, such errors could be potentially reduced to within common errors for related instrumentation such as thin-film heat transfer gauges (∼ 10 %). In fact, within regions of near-uniform temperatures, there is remarkable agreement between surface heat transfer gauges and toluene PLIF measurements with deviations within measurement uncertainty of the gauges. Moreover, the temperature rise across shock waves (nose bow shock and attached shock wave induced by a ramp) appears to be entirely consistent with isentropic theory and numerical predictions. Therefore, the technique has the potential of yielding measurements of planar temperature distributions around hypersonic bodies, where the majority of measurements to date are limited to the surface.

Acknowledgments This work was carried out under the Engineering and Physical Sciences Research council (EPSRC) grant EP/H020853/1 and made use of the EPSRC Engineering instrument Pool to borrow the iCCD spectrometer and iCCD imaging camera.

References

Anderson J Jr (2000) Hypersonic and high-temperature gas dynamics, 2nd edn. AIAA Education Series. ISBN-13: 978–1563477805

Burton CS, Noyes JWA (1968) Electronic energy relaxation in toluene vapor. J Chem Phys 49:1705–1714

Cessou A, Meier U, Stepowski D (2000) Applications of planar laser induced fluorescence in turbulent reacting flows. Meas Sci Technol 11(7):887–901

Cheung BH (2011) Tracer-based planar laser-induced fluorescence diagnostics: quantitative photophysics and time-resolved imaging. PhD Thesis, Stanford University

D'Alessio J, Lazzaro M, Massoli P, Moccia V (2002) Absorption spectroscopy of toluene pyrolysis. Opt Las Eng 37:495–508

Devillers R, Bruneaux G, Schulz C (2009) Investigation of toluene LIF at high pressure and high temperature in an optical engine. Appl Phys B 96:735–739

Einecke S, Schulz C, Sick V (2000) Measurement of temperature, fuel concentration and equivalence ratio fields using tracer LIF in IC engine combustion. Appl Phys B 71(5):717–723

Estruch-Samper D, Lawson N, Garry K (2009) Application of optical measurement techniques to supersonic and hypersonic aerospace flows. J Aerosp Eng 22(4):383–395

Estruch-Samper D, Vanstone L, Ganapathisubramani B, Hillier R (2012) Effect of roughness-induced disturbances on axisymmetric hypersonic laminar boundary layer. AIAA paper 2012–675

Faust S, Dreier T, Schulz C (2011) Temperature and bath gas composition dependence of effective uorescence lifetimes of toluene excited at 266 nm. Chem Phys 383(13):611

Fiala A, Hillier R, Mallinson SG, Wijensinghe HS (2006) Heat transfer measurement of turbulent spots in a hypersonic blunt-body boundary layer. J Fluid Mech 555:81–111

Hatanaka K, Saito T, Hirota M, Nakamura Y, Suzuki Y, Koyaguchi T (2012) Flow visualization of supersonic free jet utilizing acetone PLIF. Vis Mech Proc 2(1)

Inman JA, Bathel BF, Johansen CT, Danehy PM, Jones SB, Gragg JG, Splinter SC (2011) Nitric oxide PLIF measurements in the hypersonic materials environmental test system (HYMETS). At the 49th AIAA aerospace sciences meeting, AIAA paper 2011–1090

Johansen CT, McRae CD, Daney PM, Gallo ECA, Cantu LML, Magnotti G, Cutler AD, Rockwell RD Jr, Goyne CP, McDaniel JC (2014) OH PLIF visualization of the UVa supersonic combustion experiment: configuration A. J Vis 17(2):131–141

Koban W, Koch JD, Hanson RK, Schulz C (2004) Absorption and fluorescence of toluene vapor at elevated temperatures. Phys Chem Chem Phys 6(11):2940–2945

Koban W, Koch JD, Hanson RK, Schulz C (2005) Toluene LIF at elevated temperatures: implications for fuel-air ratio measurements. Appl Phys B 80(2):147–150

Luong M, Koban W, Schulz C (2006) Novel strategies for imaging temperature distribution using toluene LIF. J Phys Conf Ser 45:133–139

Mallinson SG, Hillier R, Jackson AP, Kirk DC, Soltani S, Zanchetta M (2000) Gun tunnel flow calibration: defining input conditions for hypersonic flow computations. Shock Waves 10:313–322

Miller VA, Gamba M, Mungal MG, Hanson RK (2013) Single- and dual-band collection toluene PLIF thermometry in supersonic flows. Exp Fluids 54:1539, 13 pp

Narayanaswamy V, Burns R, Clemens NT (2011) Kr-PLIF for scalar imaging in supersonic flows. Opt Lett 36(21):4185–4187

Needham DA, Stollery JL, Elfstrom GM (1970) Design and operation of the Imperial College Number 2 Hypersonic Gun Tunnel. Imperial College London, Aero Report 70–04

O'Byrne S, Danehy PM, Houwing AFP (2006) Investigation of hypersonic nozzle flow uniformity using NO fluorescence. Shock Waves 5:1–7

Oehlschlaeger MA, Davidson DF, Hanson RK (2007) Thermal decomposition of toluene: overall rate and branching ratio. Proc Combust Inst 31:2119

Rossmann T, Mungal MG, Hanson RK (2003) Nitric-oxide planar laser-induced fluorescence applied to low-pressure hypersonic flow fields for the imaging of mixture fraction. Appl Opt 42(33):6682–6695

Schultz DL, Jones TV (1973) Heat-transfer measurements in short-duration hypersonic facilities. AGARDograph, 165

Settles GS (2012) Schlieren and shadowgraph techniques: visualizing phenomena in transparent media (Experimental Fluid Mechanics). Springer, New York. ISBN-13: 978–3642630347

Sjoholm J, Rosell J, Li B, Richter M, Li Z, Bai X, Alden M (2012) Simultaneous visualization of OH, CH, CH_2O and toluene PLIF in a methane jet flame with varying degrees of turbulence. Proc Comb Inst 34(1):1475–1482

Strozzi C, Sotton J, Mura A, Bellenoue M (2009) Characterization of a two-dimensional temperature field within a rapid compression machine using a toluene planar laser-induced fluorescence imaging technique. Meas Sci Technol 20:125403, 13 pp

Yoo J, Mitchell D, Davidson DF, Hanson RK (2010) Planar laser-induced fluorescence imaging in shock tube flows. Exp Fluids 49:751–759

Yoo J, Mitchell D, Davidson DF, Hanson RK (2011) Near-wall imaging using toluene-based planar laser-induced fluorescence in shock tube flow. Shock Waves 21(6):523–532

Zimmermann F, Koban W, Schulz C (2006) Temperature diagnostics using laser-induced fluorescence (LIF) of toluene. OSA/LACSEA, Incline Village, Nevada, Combustion II (TuB)